J Adv Ceram

Research Article

# Self-assembled $Fe_3O_4$ nanoparticles on $V_2C$ MXene for enhanced supercapacitor and microwave absorption applications

Qixun Xia[1,2,✉], Ranlu Miao[1], Wen Guo[3], Min Xia[4], Libo Wang[1], Qianku Hu[1], Aiguo Zhou[1,✉]

Cite this article: Xia QX, Miao RL, Guo W, et al. *J Adv Ceram* 2025, **14**(3): 9221049. https://doi.org/10.26599/JAC.2025.9221049

**ABSTRACT:** Rapid advancements in modern electronic devices necessitate the development of materials that can simultaneously provide efficient energy storage and effective microwave absorption. Herein, a novel composite material was prepared via the self-assembly of $Fe_3O_4$ nanoparticles on the surface of $V_2C$ MXene. This composite exhibited characteristics suitable for supercapacitor and electromagnetic absorption applications, highlighting the synergistic relationship between energy storage and electromagnetic wave absorption capability. The electrochemical tests revealed that the specific capacity of the $V_2C$ MXene/$Fe_3O_4$ composite (42.67 mAh·g$^{-1}$) considerably improved compared with those of the raw materials. The prepared $V_2C$ MXene/$Fe_3O_4$//$V_2C$ MXene/$Fe_3O_4$ symmetric supercapacitor (SSC) demonstrated an energy density of 44.8 Wh·L$^{-1}$, a power density of 959.4 W·L$^{-1}$, and a capacity retention of 80.14% after 8000 cycles. Moreover, the $V_2C$ MXene/$Fe_3O_4$ composite exhibited an optimal reflection loss (RL) of −42.4 dB in the Ku band, with an effective absorption bandwidth of 1.9 GHz (14.6–16.5 GHz). This composite material has broad application potential in modern electronic devices owing to its high energy storage capacity and effective electromagnetic wave absorption. This dual functionality improves device performance and offers a compact solution for energy storage and effective microwave absorption.

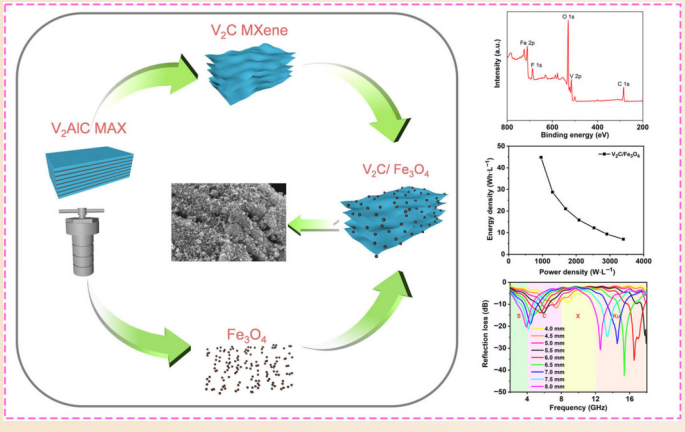


**KEYWORDS:** MXenes; $Fe_3O_4$; two-dimensional (2D) materials; supercapacitors; microwave absorption

## 1 Introduction

The increasing demand for high-performance supercapacitors and microwave absorption materials has driven extensive research into advanced composite materials. Supercapacitors exhibit high power densities, rapid charge–discharge cycles, and long lifecycles, making them among the most promising energy storage solutions. However, improving their energy density and stability remains a critical challenge. Furthermore, efficient microwave absorption is necessary to prevent interference and ensure the proper functioning of electronic devices.

Since graphene, a two-dimensional (2D) material, was discovered by Novoselov *et al.* [1] in 2004, researchers have focused on its properties and applications [2–4]. Moreover, after this discovery, researchers have increasingly focused on investigating 2D materials such as $MoS_2$, $WS_2$, $MoSe_2$, $WSe_2$, black phosphorus, hexagonal boron nitride, and MXenes [5–11]. Since their discovery in 2011, MXenes have gradually become among the most important 2D materials because of their highly porous surface area, strong electrical conductivity, high hydrophilicity, numerous functional groups, and good thermal and chemical stability, which can be attributed to their unique layered structure. MXenes can optimize several functions when combined with other materials, making them useful in numerous applications, such as in supercapacitors [12–14], microwave absorption materials [15–17], biosensors [18,19], and catalysts [20,21].

The general structure of MXenes is $M_{n+1}X_nT_x$, where M represents a transition metal element (such as Ti, V, or Mo), X represents C, N, or CN, $T_x$ represents surface functional groups (such as –O and –F), and $n$ is 1–4 [22]. MXenes are obtained via

[1] School of Materials Science and Engineering, Henan Polytechnic University, Jiaozuo 454003, China. [2] Henan Province Expressway Efficient Energy Storage Technology and Application Engineering Research Center, Zhengzhou 450121, China. [3] Department of Macromolecular Science, Fudan University, Shanghai 200438, China. [4] Henan Radio Requlation Information System Backup Center, Zhengzhou 450008, China.

✉ Corresponding authors. E-mail: Q. Xia, xqx@hpu.edu.cn; A. Zhou, zhouag@hpu.edu.cn

Received: October 30, 2024; Revised: January 28, 2025; Accepted: February 16, 2025

selective etching of layer A (A is Group III or IV A element, typically Al) of the MAX primary phase. Various etching methods, such as *in situ* etching using LiF + HCl and NaF + HCl, alkaline etching using NaOH, Lewis acid molten salt etching, and electrochemical etching and polyol etching, have been developed as improved alternatives to the etching process [23,24]. The etching agents used in these methods are milder and less toxic than HF and do not cause substantial damage to the MXene structure. Therefore, NaF + HCl was used for $V_2AlC$ MAX etching in this study. The fluoride ions in the NaF + HCl etching solution react with the aluminum layer to form $AlF_3$, effectively removing the aluminum layer to obtain highly pure $V_2C$ MXenes. Compared with KF and LiF, NaF is less chemically reactive during etching, which reduces damage to the MXene structure, allowing the materials to better maintain their layered structure.

The etching process of MXenes exposes their functional groups, such as –F, –O, and –OH, which can increase the interlayer spacing in the materials, endowing them with additional active sites and improved electrochemical properties. The excellent mechanical properties of MXenes (primarily attributed to their metal atoms), combined with their adjustable layer spacing, excellent electrical conductivity, and high volumetric specific capacitance [25], make them excellent potential electrode materials for energy storage devices. Sha *et al.* [26] prepared a TMSe@MXene nanohybrid with a specific capacity of up to 182.8 $mAh{\cdot}g^{-1}$ via *in situ* surface selenization. Zheng *et al.* [27] used chemical oxidation and etching to fabricate $Ti_3C_2$ MXene nanonets with a specific capacitance of 235 $F{\cdot}g^{-1}$ in a KOH electrolyte (6 M). The functional groups introduced during the etching process create numerous defects, increasing defect polarization, reducing conductivity, and optimizing dielectric loss and impedance matching [28,29]. Moreover, MXenes have large specific surface areas, providing abundant pathways for electromagnetic wave transmission, including multiple scattering and reflection [30,31]. Zhang *et al.* [32] developed Ni@$Ti_3C_2T_x$/polyvinyl alcohol films with a novel single-layer gradient structure, which can achieve a minimum reflection loss ($RL_{min}$) of –57.7 dB in the X band (with an effective absorption bandwidth of 3.2 GHz). Zhang *et al.* [33] synthesized a $Ti_3C_2T_x$@polydopamine@polyimide foam ($Ti_3C_2T_x$@PDA@PIF) composite with an $RL_{min}$ of –32.6 dB in the X band and an absorption capacity of > 90% for the entire X band. Therefore, MXenes are suitable for supercapacitor and microwave absorption applications [34].

In electrochemistry, transition metal oxides, such as manganese dioxide, ferroferric oxide, and titanium dioxide [35,36], and conductive polymers, such as polyaniline, polypyrrole (PPy), and polythiophene [37,38], are typically utilized as electrode materials. Reversible oxidation–reduction (redox) reactions can occur on the surfaces of transition metal oxides, enabling their use as electrode materials [39]. Among these oxides, $Fe_3O_4$ has been used in supercapacitors and microwave absorption applications because of its eco-friendliness, cost-effectiveness, and easy availability [40]. However, $Fe_3O_4$ nanostructures are prone to aggregation, limiting their development. To overcome this challenge, Li *et al.* [41] prepared a $Fe_3O_4/Fe_xS_y$ heterostructure via chemical deposition to improve the performance of lithium-sulfur batteries. Zhu *et al.* [42] prepared a nitrogen-doped carbon-supported $Fe_3O_4$ nanocomposite with satisfactory capacitance via a simple synthesis method. This nanocomposite exhibited improved electrochemical performance and no aggregation because $Fe_3O_4$ was combined with other materials with high conductivity. $Fe_3O_4$ nanoparticles exhibit high saturation magnetization, a high Curie temperature, and a considerably low dielectric constant. Their ferromagnetic properties lead to hysteresis loss and eddy current loss, effectively converting electromagnetic waves into heat energy for absorption. Furthermore, the dispersion of $Fe_3O_4$ particles induces multiple scattering of electromagnetic waves, considerably enhancing their absorption performance. Shi *et al.* [43] combined $Fe_3O_4$ with graphene to form a three-dimensional porous composite via the hydrothermal method. The formed $Fe_3O_4$/graphene composite foam exhibited a maximum absorption intensity of –47.087 dB and an absorption bandwidth of 6.7 GHz. Zhang *et al.* [44] prepared a reduced graphene oxide (RGO)/$Fe_3O_4$/$SiO_2$ terpolymer with an optimal RL of –34.36 dB and an effective absorption bandwidth of 7.76 GHz at a thickness of 2.9 mm.

In this study, $Fe_3O_4$ nanoparticles were combined with the layered accordion structure of $V_2C$ MXene via a self-assembly method. In the $V_2C$ MXene/$Fe_3O_4$ composite, $V_2C$ MXene served as a structural support for the $Fe_3O_4$ nanoparticles. Combining these two materials prevented the agglomeration of the $Fe_3O_4$ nanoparticles and ensured their full utilization in the redox reaction. Moreover, $V_2C$ MXene provided an electron migration channel to improve the magnifying capacity and power density at high charge–discharge currents, compensating for the low conductivity of $Fe_3O_4$. The specific capacity of the $V_2C$ MXene/$Fe_3O_4$ composite reached 42.67 $mAh{\cdot}g^{-1}$, which is a considerable improvement in the electrochemical performance compared with those of $V_2C$ MXene and $Fe_3O_4$ nanoparticles. In addition, the $V_2C$ MXene/$Fe_3O_4$ composite exhibited excellent microwave absorption and an acceptable bandwidth. This study provides new insights into the development of high-performance multifunctional materials through comprehensive electrochemical and electromagnetic characterization. The results of this study are expected to advance the understanding of integrated energy storage and electromagnetic absorption characteristics, offering practical solutions for modern electronic devices.

## 2 Materials and methods

### 2.1 Materials

Vanadium powders (300 mesh) and aluminum powders (200 mesh) were sourced from Beijing Xingrongyuan Technology Co., Ltd., China, whereas carbon powders (200 mesh) were obtained from Shanghai Pure Biochemical Co., Ltd., China. Ethylene glycol was obtained from Luoyang Chemical Reagent Factory, China, and polyethylene glycol was obtained from Aladdin, China. Hydrochloric acid, sodium fluoride, and ferric chloride hexahydrate were obtained from Tianjin Kemiou Chemical Reagent Co., Ltd., China. Sodium hydroxide was supplied by the Tianjin Hedong District Hongyan Reagent Factory, Tianjin, China, whereas potassium hydroxide was supplied by the Tianjin Continental Chemical Reagent Factory, Tianjin, China.

### 2.2 Preparation of $V_2C$ MXenes

Briefly, V, Al, and C powders were weighed at a ratio of 2:1.1:1 and subsequently packed into a polytetrafluoroethylene (PTFE) bottle. The powders were then uniformly mixed using a mixer for 8 h, followed by loading them into a crucible. The crucible contents were annealed at 1500 °C for 5 h in an argon atmosphere in a tube furnace (SK-B06123K, Tianjin Zhonghuan Electric Furnace Co., Ltd., China). Next, the resulting bulk structure was ground into fine powders, which were further sifted through a 500 mesh screen to obtain $V_2AlC$ MAX powders. Next, the $V_2AlC$ MAX powders (1 g) were slowly added to the etching solution (NaF (1 g), $H_2O$ (10 mL), and HCl (10 mL)), followed by ultrasonic treatment of the resulting mixture for 30 min. Thereafter, the ultrasonically treated mixture was heated to 90 °C for 7 d.

Subsequently, the obtained suspension was centrifuged, washed, and vacuum-dried at 60 °C for 10 h to obtain $V_2C$ MXene.

### 2.3 Preparation of $Fe_3O_4$ nanoparticles

$FeCl_3{\cdot}6H_2O$ (1.5 g) and NaOH (0.478 g) were added to ethylene glycol (44.45 mL), followed by the addition of polyethylene glycol (10 mL). The mixture was stirred for 60 min and transferred to the inner lining of a high-pressure reactor (100 mL) at 200 °C. The reaction was conducted for 8, 12, and 16 h. $Fe_3O_4$ nanoparticles were subjected to (i) centrifugation in deionized water and (ii) drying at 60 °C for 12 h to obtain three types of $Fe_3O_4$ nanoparticles, $Fe_3O_4$-8, $Fe_3O_4$-12, and $Fe_3O_4$-16 (8, 12, and 16 denote the reaction times in hours). These different reaction times were used to study the effects of the reaction time on the size, morphology, and properties of the $Fe_3O_4$ nanoparticles.

### 2.4 Synthesis of $V_2C$ MXene/$Fe_3O_4$

$Fe_3O_4$ (0.1 g) and $V_2C$ MXene (0.1 g) were dissolved in ethanol (50 mL) via magnetic stirring for 60 min. Subsequently, the obtained suspension was subjected to ultrasonic treatment for 2 h. Next, the ultrasonically treated suspension was centrifuged at 8500 r·min$^{-1}$ for 30 min and vacuum-dried at 60 °C for 12 h to obtain $V_2C$ MXene/$Fe_3O_4$.

### 2.5 Electrode manufacturing

Nickel foam, measuring 2 cm by 4 cm, was sonicated in a 6-M hydrochloric acid solution for 5 min. Next, it was sonicated in deionized water for ~10 min to remove any residual hydrochloric acid from the surface. The nickel foam was subsequently subjected to ultrasonic cleaning with ethanol and then dried, after which it was prepared for use as a substrate in a three-electrode system. The active materials were prepared by thoroughly mixing $V_2C$ MXene/$Fe_3O_4$ (80 wt%) with carbon black (10 wt%) and a PTFE binder (10 wt%) at a mass ratio of 8:1:1. This active material was then coated onto the pretreated nickel foam substrate via a slurry coating process. The coating was applied to two-thirds of the nickel foam, covering an area of 1 cm$^2$. The nickel foam was then folded to ensure that it completely encapsulated the active materials, preventing any leakage during testing. Finally, the encapsulated materials were vacuum-dried for 10 h at 60 °C to obtain the working electrodes.

A similar procedure was followed to prepare the positive and negative electrodes for assembling a supercapacitor device. The nickel foam was cut into circular pieces with a diameter of 1.6 cm, and after undergoing the same treatments, the active materials were directly coated on the center of each circular nickel foam piece. The circular nickel foam pieces were then placed in a vacuum drying oven (DZF-6020AB, Beijing Zhongxing Weiye Reagent Instrument Co., Ltd., China) to produce positive and negative electrodes for the supercapacitor device. The weight ratio of the active materials to the nickel foam (surface density = 350 g·m$^{-2}$) was found to be 1:8. Finally, the positive and negative electrodes were arranged and packaged to assemble the supercapacitor device.

### 2.6 Material characterization

An X-ray diffractometer (XRD; Rigaku, SmartLab, Tokyo, Japan) was used to analyze the crystal structure of the sample. The surface morphology and microstructure of the MXenes loaded with $Fe_3O_4$ nanoparticles were characterized via a field-emission scanning electron microscope (ZEISS Gemini 300, Carl Zeiss NTS GmbH, Germany). The microstructure of the $V_2C$ MXene/$Fe_3O_4$ was further analyzed via a transmission electron microscope (TEM; JEM 2100F, JEOL, Japan). An X-ray photoelectron spectroscope (XPS; ESCALAB 250Xi, Thermo Fisher Scientific, USA) was employed to determine the surface chemical composition of the composite. Avantage software was used to analyze the chemical composition, with the C 1s peak at 284.8 eV employed as a reference.

#### 2.6.1 *Electrochemical testing*

Electrochemical impedance spectroscopy, cyclic voltammetry (CV), galvanostatic charge–discharge (GCD), and cycle life performance tests were performed on the materials via an electrochemical workstation (Ivium, Vertical.C. IS, the Netherlands). KOH (1 M) was used as the electrolyte, and Hg/HgO and platinum foil were used as the reference and counter electrodes, respectively. The CV and GCD curves were obtained at different sweep rates and current rates, respectively, within a voltage window of 0–0.6 V. The cycle stability was measured at a current density of 3 A·g$^{-1}$. Equation (1) was used to calculate the specific capacity of the electrodes ($C_s$) [45,46]:

$$C_s = \frac{I\Delta t}{m} \tag{1}$$

where $C_s$ (mAh·g$^{-1}$) represents the specific capacity of the electrode, $I$ (mA) is the discharge current applied during the test, $m$(g) is the mass of the active materials, and $\Delta t$ (h) is the discharge time.

Symmetric supercapacitors (SSCs) with $V_2C$ MXene/$Fe_3O_4$//$V_2C$ MXene/$Fe_3O_4$ structures were prepared, and their specific capacity ($c_d$) was calculated on the basis of their electrochemical test results via Eq. (2) [47,48]:

$$c_d = \frac{I\Delta t}{M} \tag{2}$$

where $M$ (g) represent the total mass of the positive and negative active materials.

The $V_2C$ MXene/$Fe_3O_4$ composite was pressed into a sheet (area = 1 cm$^2$) under a pressure of 20 MPa, and its density was calculated on the basis of its measured mass to be 2.16 g·cm$^{-3}$. The volumetric energy density ($E$; Wh·L$^{-1}$) and the volumetric power density ($P$; W·L$^{-1}$) of the SSC device were calculated on the basis of the GCD curve via Eqs. (3) and (4) [49]:

$$E = \frac{\rho \int IV\mathrm{d}t}{3.6M} \tag{3}$$

$$P = \frac{E}{\Delta t} \tag{4}$$

where $\rho$ (g·cm$^{-3}$) represents the density of the active materials, and $V$ (V) denotes the voltage window.

#### 2.6.2 *Wave absorption test*

The permittivity (of which $\varepsilon'$ is the real part and $\varepsilon''$ is the imaginary part) and magnetic permeability (of which $\mu'$ is the real part and $\mu''$ is the imaginary part) of the $V_2C$ MXene/$Fe_3O_4$ composites were tested via the coaxial method via a vector network distributor (E5071C, Agilent, USA). The $V_2C$ MXene/$Fe_3O_4$ composites were uniformly mixed with paraffin wax at a 1:1 ratio. The resulting mixture was then molded into a coaxial ring (thickness ≈ 2.0 mm, inner diameter = 3.04 mm, and outer diameter = 7.0 mm). The microwave absorption properties of the $V_2C$ MXene/$Fe_3O_4$ composites were tested in the frequency range of 2–18 GHz. The instrument was evaluated in magnetic mode, utilizing a calibration standard with a precision of ±0.005. The RL of the composite at different thicknesses was calculated via transmission line theory [50–52] via Eqs. (5) and (6) as

$$Z_{in} = Z_0 \left(\mu_r/\varepsilon_r\right)^{\frac{1}{2}} \tanh\left(j\frac{2\pi df}{c}\left(\mu_r/\varepsilon_r\right)^{\frac{1}{2}}\right) \quad (5)$$

$$RL = 20\log\left|\frac{Z_{in} - Z_0}{Z_{in} + Z_0}\right| \quad (6)$$

where $Z_{in}$ denotes the normalized input impedance of the materials, $Z_0$ represents the free-space characteristic impedance, $\mu_r$ is defined as relative complex permeability, $\varepsilon_r$ signifies the relative complex permittivity, $d$ is given by the thickness of the wave-absorbing materials, $f$ relates to the frequency, $j$ symbolizes phase shift in wave propagation, and $c$ corresponds to the speed of light.

The absorbing attenuation constant ($M_\eta$) and wave impedance matching ($\alpha$) were calculated via Eqs. (7) and (8), respectively:

$$M_\eta = \frac{2\eta'}{|\eta|^2 + 1} \quad (7)$$

$$\alpha = \frac{\sqrt{2}\pi f}{c}\{(\mu''\varepsilon'' - \mu'\varepsilon') + [(\mu''\varepsilon'' - \mu'\varepsilon')^2 + (\mu''\varepsilon'' + \mu'\varepsilon')^2]^{\frac{1}{2}}\}^{\frac{1}{2}} \quad (8)$$

$$\eta = \left(\mu_r/\varepsilon_r\right)^{\frac{1}{2}} \quad (9)$$

where $\eta$ represents the relative wave impedance, and $\eta'$ is its real part.

## 3 Results and discussion

Figure 1 shows the preparation of the self-assembled $V_2C$ MXene/$Fe_3O_4$ composite. The $V_2C$ MXene materials were obtained by etching $V_2AlC$ via a NaF + HCl etching solution, while the $Fe_3O_4$ nanoparticles were synthesized via a simple hydrothermal method. The $V_2C$ MXene materials and $Fe_3O_4$ nanoparticles were subsequently composited via the self-assembly method to obtain a $V_2C$ MXene/$Fe_3O_4$ composite.

The micromorphological analysis and crystal structure characterization of the $Fe_3O_4$ nanoparticles synthesized at different reaction times are shown in Fig. 2. Figure 2(a) displays the SEM image of $Fe_3O_4$ nanoparticles synthesized for 8 h. The micrograph reveals co-existence of larger particles with smaller ones, which can be attributed to incomplete growth due to the short reaction time. This phenomenon suggests that $Fe_3O_4$ was still in the nucleation stage at this reaction duration. Figure 2(b) shows the $Fe_3O_4$ nanoparticles synthesized for 12 h. Compared with the $Fe_3O_4$-8 nanoparticles, the nanoparticles exhibit a more regular structure and a considerably larger particle size. Figure 2(c) shows the $Fe_3O_4$ nanoparticles synthesized for 16 h. Owing to the prolonged reaction time, the particle surface is covered with a layer of smaller nanoparticles, which could compromise the surface integrity. The particle size analysis results indicate that the average particle sizes of the $Fe_3O_4$-8, $Fe_3O_4$-12, and $Fe_3O_4$-16 nanoparticles are 111, 202, and 155 nm, respectively. The XRD patterns of $Fe_3O_4$ synthesized at different reaction times are shown in Fig. 2(d). The peaks of the three samples match the JCPDS#19-0629 standard peaks (purple pattern), indicating that $Fe_3O_4$ nanoparticles synthesized for 12 h had an optimized microstructure. Thus, $Fe_3O_4$ synthesized for 12 h was used in all $V_2C$ MXene/$Fe_3O_4$ composites.

A scanning electron microscope (SEM) was used to analyze the morphological characteristics of the $V_2C$ MXene/$Fe_3O_4$ composite. The SEM image of $V_2C$ MXene (Fig. 3(a)) shows an layer structure, indicating that the Al atomic layer in the MAX original phase was selectively etched. The SEM image of $Fe_3O_4$ (Fig. 3(b)) shows the formation of a $Fe_3O_4$ nanoparticle structure with clear agglomeration due to its inherent magnetic properties. The SEM image of the $V_2C$ MXene/$Fe_3O_4$ composite (Fig. 3(c)) shows the successful attachment of the $Fe_3O_4$ particles to the lamellar structure of $V_2C$ MXene, increasing the surface roughness of the $V_2C$ MXene structure. This SEM image confirms that few particles enter the $V_2C$ MXene layer, further expanding its interlayer distance and facilitating ion transport in the electrolyte. The energy-dispersive X-ray spectroscopy (EDS) patterns shown in Fig. 3(d) confirm the presence of C, V, O, and Fe in the $V_2C$ MXene/$Fe_3O_4$ composite. These results indicate the uniform distribution of the $Fe_3O_4$ nanoparticles on the $V_2C$ MXene.

The micromorphology of the $V_2C$ MXene/$Fe_3O_4$ composite was analyzed via TEM (Fig. 3(e)). The lamellar structure of $V_2C$ can be clearly observed in the TEM image shown in Fig. 3(e). Moreover, this pattern shows that the $Fe_3O_4$ particles are attached to the nanosheet structure, which is in good agreement with the SEM analysis results. The selected area electron diffraction pattern shown in the inset in Fig. 3(e) demonstrates the crystalline nature of the $V_2C$ MXene/$Fe_3O_4$ composite. The high-resolution TEM (HRTEM) image of $Fe_3O_4$ presented in Fig. 3(f) shows crystal plane spacings of 0.219, 0.269, and 0.200 nm, which correspond to the (222), (311), and (400) crystal planes of $Fe_3O_4$ (JCPDS#19-0629), respectively.

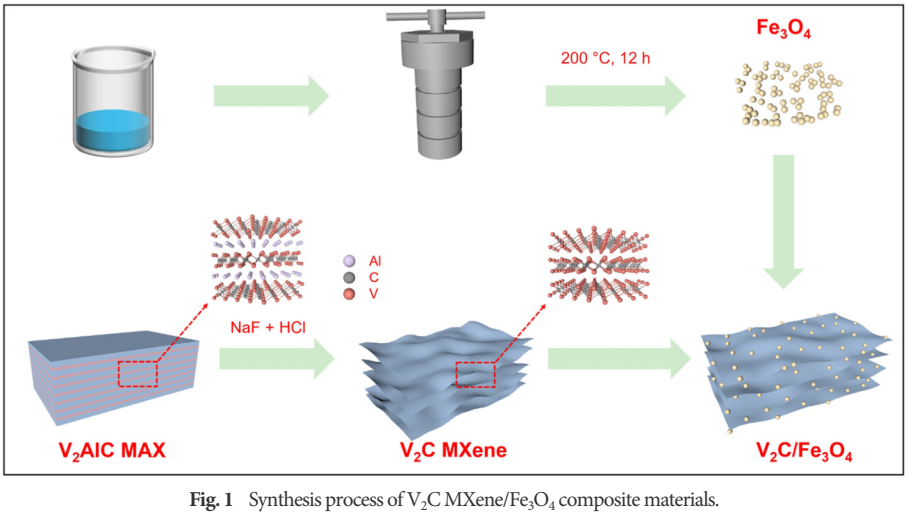


**Fig. 1** Synthesis process of $V_2C$ MXene/$Fe_3O_4$ composite materials.

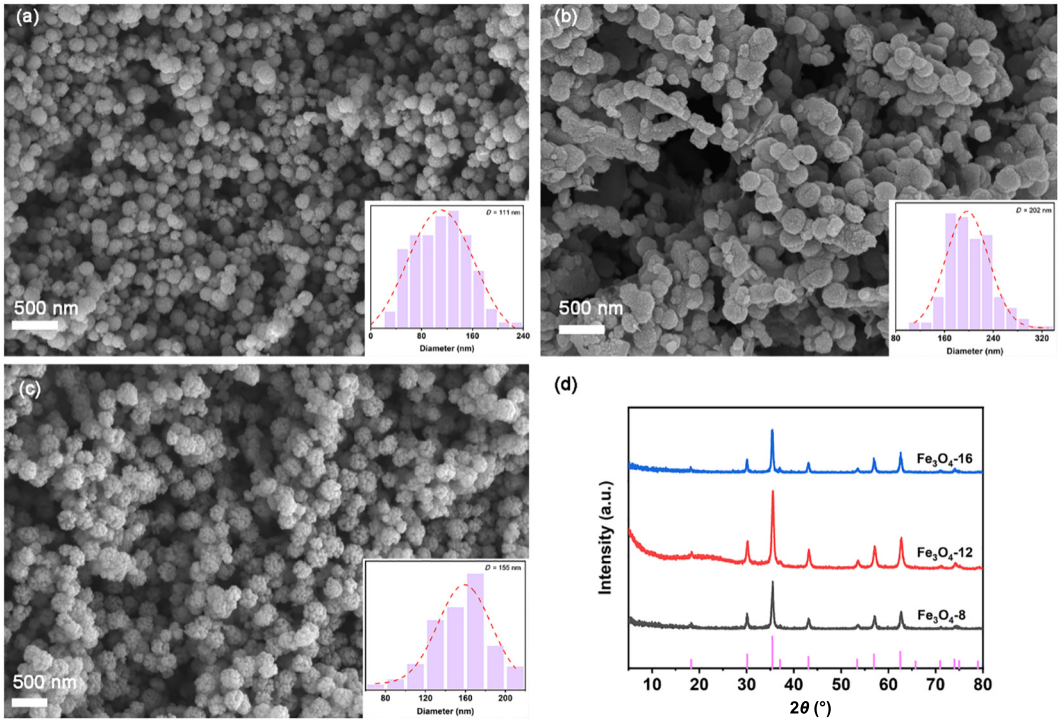


**Fig. 2** SEM images of (a) $Fe_3O_4$-8, (b) $Fe_3O_4$-12, and (c) $Fe_3O_4$-16. (d) XRD patterns of $Fe_3O_4$-8, $Fe_3O_4$-12, and $Fe_3O_4$-16.

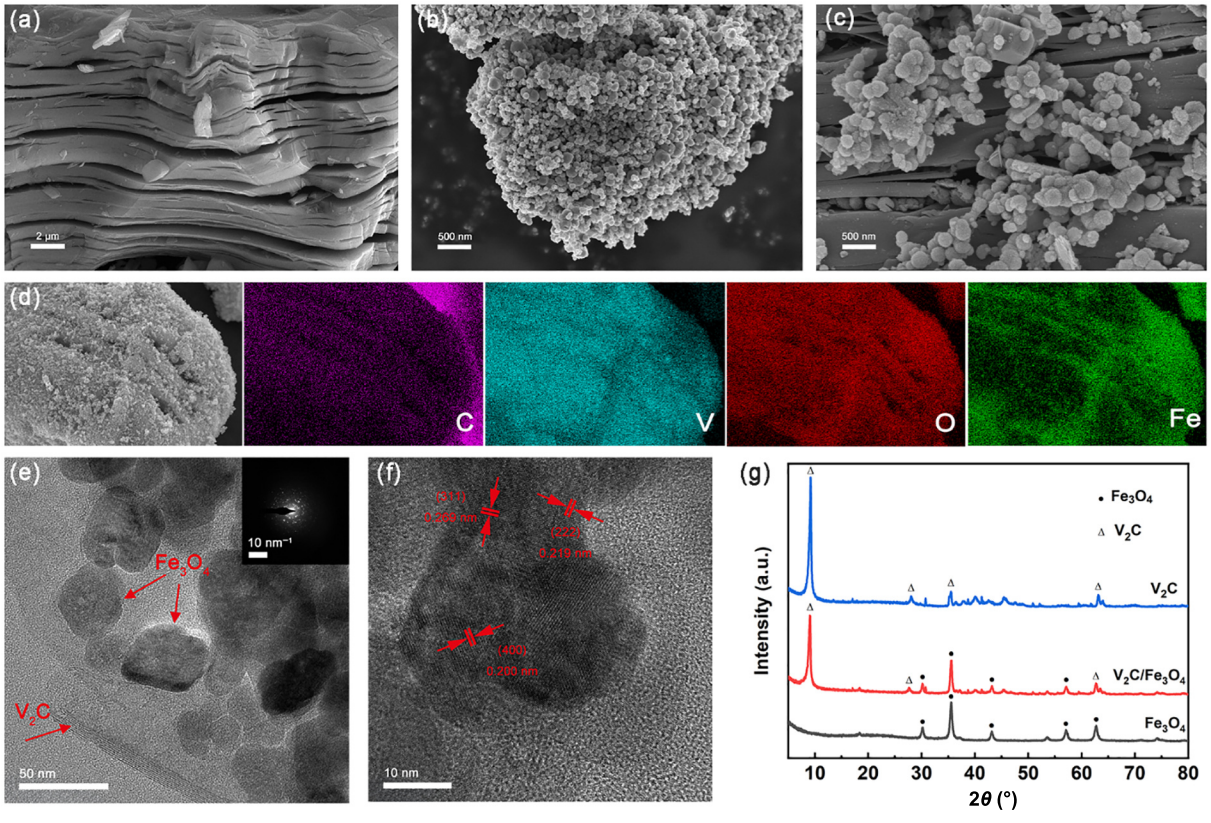


**Fig. 3** SEM images of (a) $V_2C$, (b) $Fe_3O_4$, and (c) $V_2C$ MXene/$Fe_3O_4$ composite. (d) EDS patterns of $V_2C$ MXene/$Fe_3O_4$ composite. (e) TEM image and selected area electron diffraction maps of $V_2C$ MXene/$Fe_3O_4$ composite. (f) HRTEM image of $Fe_3O_4$. (g) XRD patterns of $Fe_3O_4$, $V_2C$, and $V_2C$ MXene/$Fe_3O_4$ electrodes.

The XRD patterns of $Fe_3O_4$, $V_2C$, and $V_2C$ MXene/$Fe_3O_4$ are shown in Fig. 3(g). These patterns provide information regarding the purity and crystallinity of the synthesized $Fe_3O_4$ nanoparticles. The diffraction peaks observed at $2\theta$ = 30.09°, 35.42°, 43.05°, 56.94°, and 62.51° correspond to the (220), (311), (400), (511), and (440) crystal planes, respectively. These peaks match the peaks reported in the standard XRD diffraction card of $Fe_3O_4$ (JCPDS#19-0629), indicating that the synthesized $Fe_3O_4$ has a face-centered cubic crystal structure [53]. The XRD pattern (red pattern) of the $V_2C$ MXene/$Fe_3O_4$ composite indicates the

presence of diffraction peaks corresponding to the (220), (311), (400), and (511) crystal planes, confirming that the $V_2C$ MXene/$Fe_3O_4$ composite contains $Fe_3O_4$. The XRD pattern (blue pattern) of $V_2C$ MXene shows a prominent diffraction peak at $2\theta$ = 9.21° (a characteristic peak of MXene materials) corresponding to the (002) crystal plane. Several peaks with intensities lower than that of this prominent peak are also observed. The peaks observed at $2\theta$ = 30.71° and 38.70° match the characteristic peaks of $Na_5Al_3F_{14}$ (PDF#30-1144) and correspond to the (202) and (213) crystal planes, respectively. Moreover, the peak observed at $2\theta$ = 41.26° matches the characteristic peak of $V_2AlC$ MAX (PDF#29-0101) and corresponds to the (103) crystal plane. These results suggest that a small amount of cone cryolite is formed during the reactions of $Na^+$, $F^-$, and Al in $V_2AlC$ MAX during the etching process of $V_2C$ MXene and that some of the original $V_2AlC$ MAX phase remains incompletely etched. These findings are consistent with those of previous studies [54]. In the XRD pattern of the $V_2C$ MXene/$Fe_3O_4$ composite (red spectra), the (002) characteristic peak shifts to $2\theta$ = 9.01°, indicating an increase in the interplanar spacing from 0.959 to 0.981 nm. In addition, all the characteristic peaks of $V_2C$ in the $V_2C$ MXene/$Fe_3O_4$ composite shift to a smaller angle, indicating that the incorporation of the $Fe_3O_4$ nanoparticles increases the interlayer spacing of $V_2C$ MXene, which is in good agreement with the SEM analysis results. The increase in the layer spacing of the $V_2C$ MXene/$Fe_3O_4$ composite facilitates ion transport, resulting in improved electrochemical properties.

The surface chemical composition and state of the $V_2C$ MXene/$Fe_3O_4$ composite were examined via XPS (Fig. 4). The XPS full-scan spectrum presented in Fig. 4(a) shows five peaks corresponding to Fe, F, O, V, and C. The high-resolution V 2p spectra shown in Fig. 4(b) can be fitted into four peaks: V–O (516.7 and 524.2 eV) and V–C (514.0 and 521.7 eV). The C 1s peaks (Fig. 4(c)) [55] observed at 282.4, 284.8, 286.3, and 288.5 eV correspond to the electronic states of C–V, C–C, C–O, and O–C=O, respectively. The O 1s spectra presented in Fig. 4(d) mainly show the Fe–O peak at 530.3 eV and the V–O–H peak at 531.6 eV, which proves the occurrence of –OH termination. The F 1s spectrum presented in Fig. 4(e) shows a strong signal at 688.6 eV, confirming the presence of fluoro-functional groups, which form C–V–$F_x$ bonds, on the $V_2C$ surface. The two asymmetric Fe 2p peaks (Fig. 4(f)) observed at 724.4 and 711.2 eV are attributed to the Fe $2P_{1/2}$ and Fe $2P_{3/2}$ orbitals, respectively. The Fe $2p_{3/2}$ peaks are deconvoluted into $Fe^{3+}$ and $Fe^{2+}$ peaks at 714.5 and 711.3 eV, respectively. Similarly, the Fe $2p_{1/2}$ peaks are deconvolved into $Fe^{3+}$ and $Fe^{2+}$ peaks at 727.5 and 724.1 eV, respectively. In addition, two satellite peaks are observed at 719.2 and 732.7 eV. These results confirm the abundance of active sites in the $V_2C$ MXene/$Fe_3O_4$ composite. This abundance increases its performance and cycling stability.

### 3.1 Electrochemical performance

The electrochemical properties of the $Fe_3O_4$ nanoparticles synthesized at different reaction times were tested. Figures 5(a)–5(c) show the CV curves of the $Fe_3O_4$ nanoparticles at scan rates of 5–50 mV·$s^{-1}$, where the redox peaks of the electrode material are observed. Figures 5(d)–5(f) display the GCD curves of the $Fe_3O_4$ nanoparticles at current densities of 1–5 A·$g^{-1}$. The charge–discharge times for $Fe_3O_4$-8, $Fe_3O_4$-12, and $Fe_3O_4$-16 are 64.4, 107.6, and 72.8 s, respectively.

Figure 6 shows the CV, GCD, cycle life, and specific capacity of the $Fe_3O_4$ nanoparticles synthesized at different reaction times. A comparison of the CV curves indicates that the $Fe_3O_4$ nanoparticles synthesized for 12 h have the largest integral area, indicating that they have the largest charge storage capacity and enhanced reactivity. The GCD curve reveals that $Fe_3O_4$-12 has the longest charge–discharge duration at a current density of 1 A·$g^{-1}$, suggesting remarkable energy density. The cycle life of the $Fe_3O_4$ electrode tested at a current density of 3 A·$g^{-1}$ is presented in Fig. 6(c). After 5000 cycles, the capacity retention rates of $Fe_3O_4$-8, $Fe_3O_4$-12, and $Fe_3O_4$-16 are 75.8%, 93.7%, and 70.6%, respectively. The specific capacities of the $Fe_3O_4$ samples calculated via Eq. (1) are shown in Fig. 6(d). At a current density ($j$) of 1 A·$g^{-1}$, the specific capacities of $Fe_3O_4$-8, $Fe_3O_4$-12, and $Fe_3O_4$-16 are 8.44, 12.67, and 9.06 mAh·$g^{-1}$, respectively. Thus, $Fe_3O_4$ synthesized for 12 h demonstrates exceptional performance in electrochemical applications.

The electrochemical performances of the $V_2C$, $Fe_3O_4$, and $V_2C$

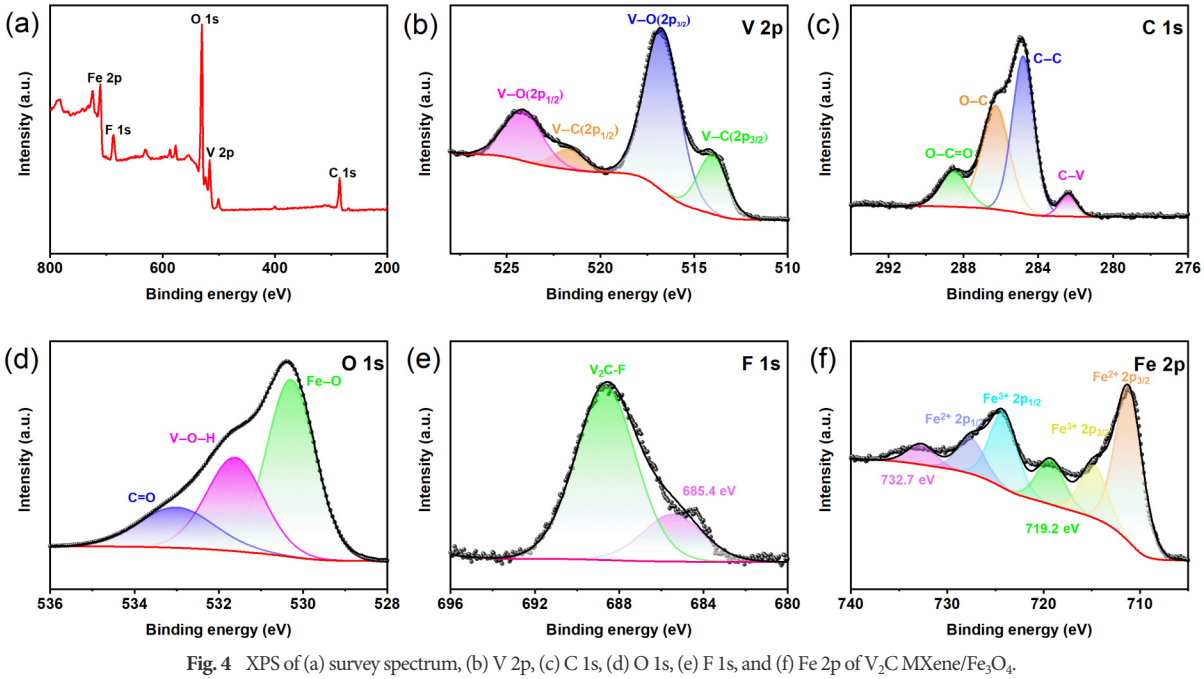


**Fig. 4** XPS of (a) survey spectrum, (b) V 2p, (c) C 1s, (d) O 1s, (e) F 1s, and (f) Fe 2p of $V_2C$ MXene/$Fe_3O_4$.

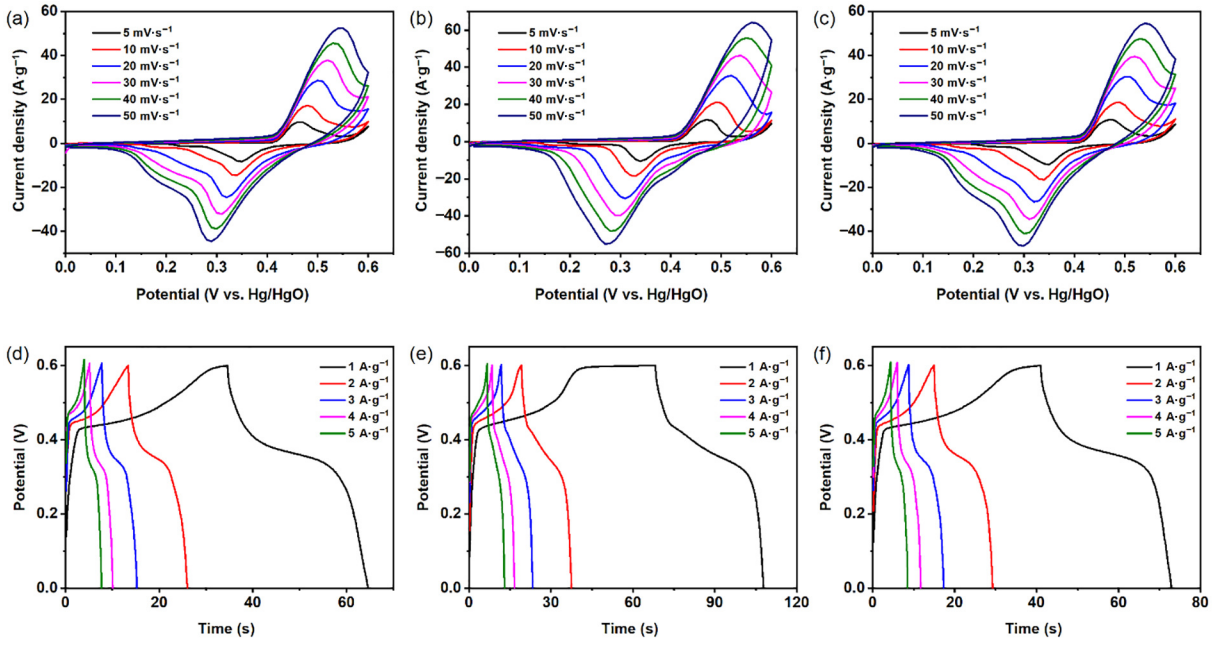


**Fig. 5** CV curves of (a) $Fe_3O_4$-8, (b) $Fe_3O_4$-12, and (c) $Fe_3O_4$-16 electrodes at different current densities. GCD curves of (d) $Fe_3O_4$-8, (e) $Fe_3O_4$-12, and (f) $Fe_3O_4$-16 electrodes at different current densities.

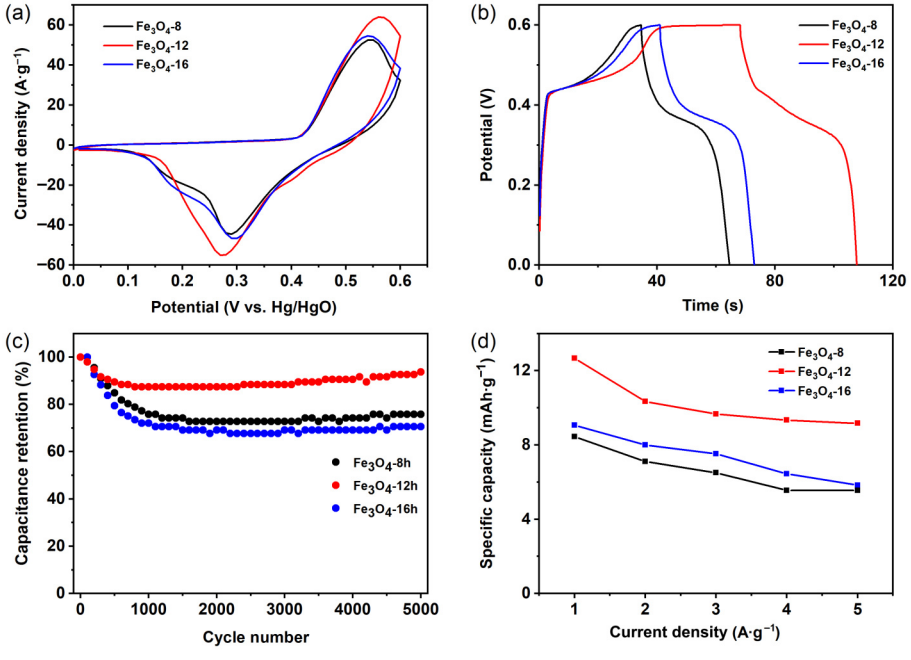


**Fig. 6** (a) Comparative CV curves at a scan rate of 50 mV·s$^{-1}$, (b) comparative GCD curves at a current density of 1 A·g$^{-1}$, (c) cycling performance, and (d) specific capacity vs. current density of $Fe_3O_4$ synthesized at different reaction times.

MXene/$Fe_3O_4$ electrodes were tested. Figures 7(a)–7(c) show the CV curves of $Fe_3O_4$, $V_2C$, and $V_2C$ MXene/$Fe_3O_4$ at different scan rates (5–50 mV·s$^{-1}$) in a KOH (1 M) electrolyte. The alkaline environment created with KOH promotes ion diffusion, which enhances charge transfer in electrochemical reactions. The presence of $OH^-$ in the solution can increase the mobility of ions and accelerate their intercalation rate in the MXene layered structure. Moreover, $OH^-$ can interact with transition metals and functional groups in the MXene structure, optimizing the chemical properties of the MXene. The redox current clearly increases with increasing scanning rate, indicating the good electrochemical reversibility of the three samples. In addition, the redox peaks of the prepared electrode gradually disappear with systematic shifts to the right and left sides with increasing scanning rates, indicating high reversibility. The comparison of the CV profile shown in Fig. 7(d) reveals that the $V_2C$ MXene/$Fe_3O_4$ electrode has the largest integral CV area, which can be attributed to the synergetic effect between $V_2C$ and $Fe_3O_4$.

Figures 8(a)–8(c) show the GCD curves of $Fe_3O_4$, $V_2C$, and $V_2C$ MXene/$Fe_3O_4$ at different current densities in a voltage window of 0–0.6 V. The GCD curves of the three samples at 1 A·g$^{-1}$ are compared in Fig. 8(d). The charge–discharge times of $Fe_3O_4$, $V_2C$, and $V_2C$ MXene/$Fe_3O_4$ are 107.8, 161.4, and 324.2 s, respectively. The charge–discharge time of the $V_2C$ MXene/$Fe_3O_4$ composite electrode is longer than those of the $Fe_3O_4$ and $V_2C$ electrodes at 1 A·g$^{-1}$, indicating the enhanced electrochemical

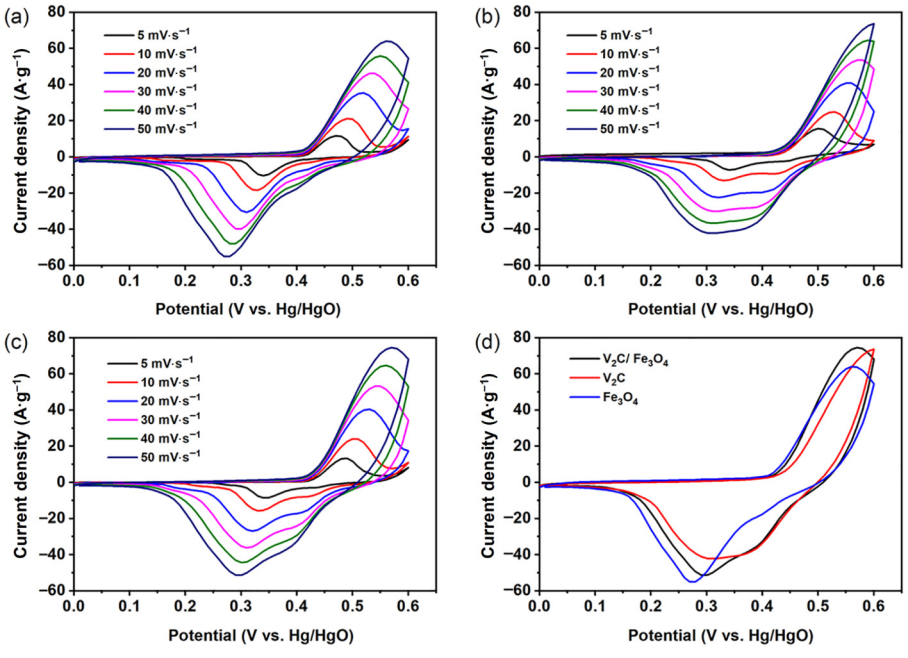


**Fig. 7** CV curves of (a) $Fe_3O_4$, (b) $V_2C$, and (c) $V_2C$ MXene/$Fe_3O_4$ electrodes at different scanning rates (5–50 mV·s$^{-1}$). (d) Comparative CV curves of $Fe_3O_4$, $V_2C$, and $V_2C$ MXene/$Fe_3O_4$ electrodes at a scan rate of 50 mV·s$^{-1}$.

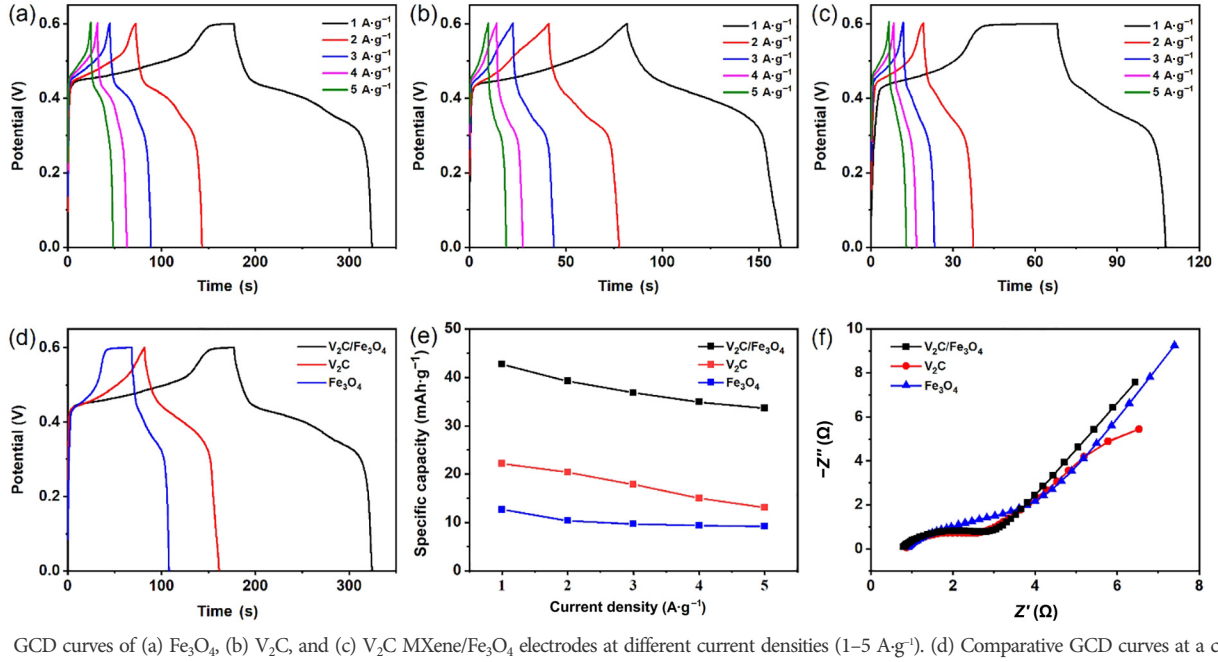


**Fig. 8** GCD curves of (a) $Fe_3O_4$, (b) $V_2C$, and (c) $V_2C$ MXene/$Fe_3O_4$ electrodes at different current densities (1–5 A·g$^{-1}$). (d) Comparative GCD curves at a current density of 1 A·g$^{-1}$, (e) specific capacity vs. current density, and (f) electrochemical impedance spectroscopy of $V_2C$, $Fe_3O_4$, and $V_2C$ MXene/$Fe_3O_4$ electrodes.

performance of the $V_2C$ MXene/$Fe_3O_4$ composite electrode. The synergetic effects between $V_2C$ MXene and $Fe_3O_4$ enhance the specific capacity of the composite material. Owing to their high electrical conductivity, large specific surface area, and excellent ion storage capability, $V_2C$ MXenes provide a strong framework for efficient charge transfer. Furthermore, the high specific capacitance of the $Fe_3O_4$ nanoparticles and their ability to undergo reversible Faradaic reactions improved the overall electrochemical performance of the composite. The interaction between $V_2C$ and $Fe_3O_4$ creates a favorable environment for both capacitive and pseudocapacitive charge storage mechanisms. The conductive MXene phase improves electron transport, whereas the $Fe_3O_4$ phase facilitates the storage of charge through redox reactions, leading to an overall increase in the specific capacity of the device. In addition, the dispersion of $Fe_3O_4$ within the MXene matrix helps reduce the agglomeration of the $Fe_3O_4$ nanoparticles, improving the stability and specific capacity of the composite during charge–discharge cycles. The combined effect of these two materials results in improved electrochemical performance, as reflected in the CV and GCD results.

The GCD data of the three samples were calculated via Eq. (1) to draw a comparison diagram of the specific capacity at different current densities (Fig. 8(e)). As shown in Fig. 8(e), at a current density of 1 A·g$^{-1}$, the specific capacities of the three materials are in the following order: $Fe_3O_4$ (12.67 mAh·g$^{-1}$) < $V_2C$ (22.11 mAh·g$^{-1}$) < $V_2C$ MXene/$Fe_3O_4$ (42.67 mAh·g$^{-1}$), with the

$V_2C$ MXene/$Fe_3O_4$ composite material exhibiting the highest specific capacity. The specific capacity of the material decreases with increasing current density. At a current density of 5 A·g$^{-1}$, the capacity retentions of $V_2C$ MXene/$Fe_3O_4$, $V_2C$, and $Fe_3O_4$ are 78.77%, 59.07%, and 72.38%, respectively. Thus, the $V_2C$ MXene/$Fe_3O_4$ composite has a higher capacity and better magnification performance than the other two samples.

The ion transport characteristics of the electrolytes of the $V_2C$ MXene, $Fe_3O_4$, and $V_2C$ MXene/$Fe_3O_4$ electrodes were studied via the resistance method, and the results were fitted via Zview software. Electrochemical impedance spectroscopy was then conducted on the $V_2C$ MXene, $Fe_3O_4$, and $V_2C$ MXene/$Fe_3O_4$ electrodes (Fig. 8(f)). The semicircles in the high-frequency region reflect the charge transfer resistance ($R_{ct}$), and the slope in the low-frequency region signifies the Warburg resistance ($Z_w$). The $R_{ct}$ values of the $V_2C$ MXene, $Fe_3O_4$, and $V_2C$ MXene/$Fe_3O_4$ electrodes are 2.4, 3.9, and 2.3 Ω, respectively. The addition of the $Fe_3O_4$ nanoparticles reduces the electrochemical impedance of the $V_2C$ MXene material and promotes charge transfer among the layers of $V_2C$ MXene. Compared with the $V_2C$ MXene electrode, the $V_2C$ MXene/$Fe_3O_4$ electrode has a larger $Z_w$, suggesting a higher diffusion rate of the electrolyte in the $V_2C$ MXene/$Fe_3O_4$ composite electrode. These results demonstrate the excellent electrical conductivity of the $V_2C$ MXene/$Fe_3O_4$ electrode.

The cycle stability performance of the $V_2C$ MXene/$Fe_3O_4$ composite electrode was further studied. The cycle life of the three samples was tested at 3 A·g$^{-1}$. The results are shown in Fig. 9(a). As shown in this figure, $V_2C$ MXenes exhibit satisfactory cyclic stability and a capacity retention rate of 74.2% at 5000 cycles. The capacity retention rate of the $V_2C$ MXene/$Fe_3O_4$ composite remains at ~100%, with marginal fluctuations. The Coulombic efficiencies were obtained from the GCD cycling tests (Fig. 9(b)), with the $V_2C$ MXene/$Fe_3O_4$ composite consistently maintaining efficiencies of ~99%. These results indicate that the $V_2C$ MXene/$Fe_3O_4$ composite has excellent electrochemical stability. Moreover, the results show that the decoration of the $V_2C$ MXene nanosheets with the $Fe_3O_4$ nanoparticles enhances the electrochemical performance of the composite. Furthermore, the prepared $V_2C$ MXene/$Fe_3O_4$ electrodes demonstrate superior specific capacity compared with other MXene-based and $Fe_3O_4$-based composites (Table 1).

To further investigate the electrochemical properties and practical application of the $V_2C$ MXene/$Fe_3O_4$ composite, an SSC device comprising the $V_2C$ MXene/$Fe_3O_4$ composite as the anode and cathode material was constructed. Figure 9(c) exhibits the CV curves of the $V_2C$ MXene/$Fe_3O_4$//$V_2C$ MXene/$Fe_3O_4$ SSC device at a scan rate of 5–50 mV·s$^{-1}$ and a voltage window of 0–1.6 V. The shape of the CV curves of the SSC device remains approximately rectangular, demonstrating that the synthesized $V_2C$ MXene/$Fe_3O_4$ material has excellent electrochemical performance with good capacity and rate performance. The GCD curves of the $V_2C$ MXene/$Fe_3O_4$ SSC device at current densities of 0.2–0.8 A·g$^{-1}$ (Fig. 9(d)) show a nonlinear relationship, confirming their pseudocapacitive behavior. The specific capacitances of the $V_2C$ MXene/$Fe_3O_4$ SSC device at current densities of 0.2, 0.3, 0.4, 0.5, 0.6, 0.7, and 0.8 A·g$^{-1}$ are measured on the basis of the GCD curves to be 9.34, 6.63, 5, 3.81, 3.9, 2.26, and 1.64 mAh·g$^{-1}$, respectively, corresponding to Cullen efficiencies of 78.9%, 87.9%, 90.7%, 91.3%, 89.7%, 92.1%, and 88.1%, respectively (Fig. 9(e)).

As shown in Fig. 9(f), the volumetric power density and the

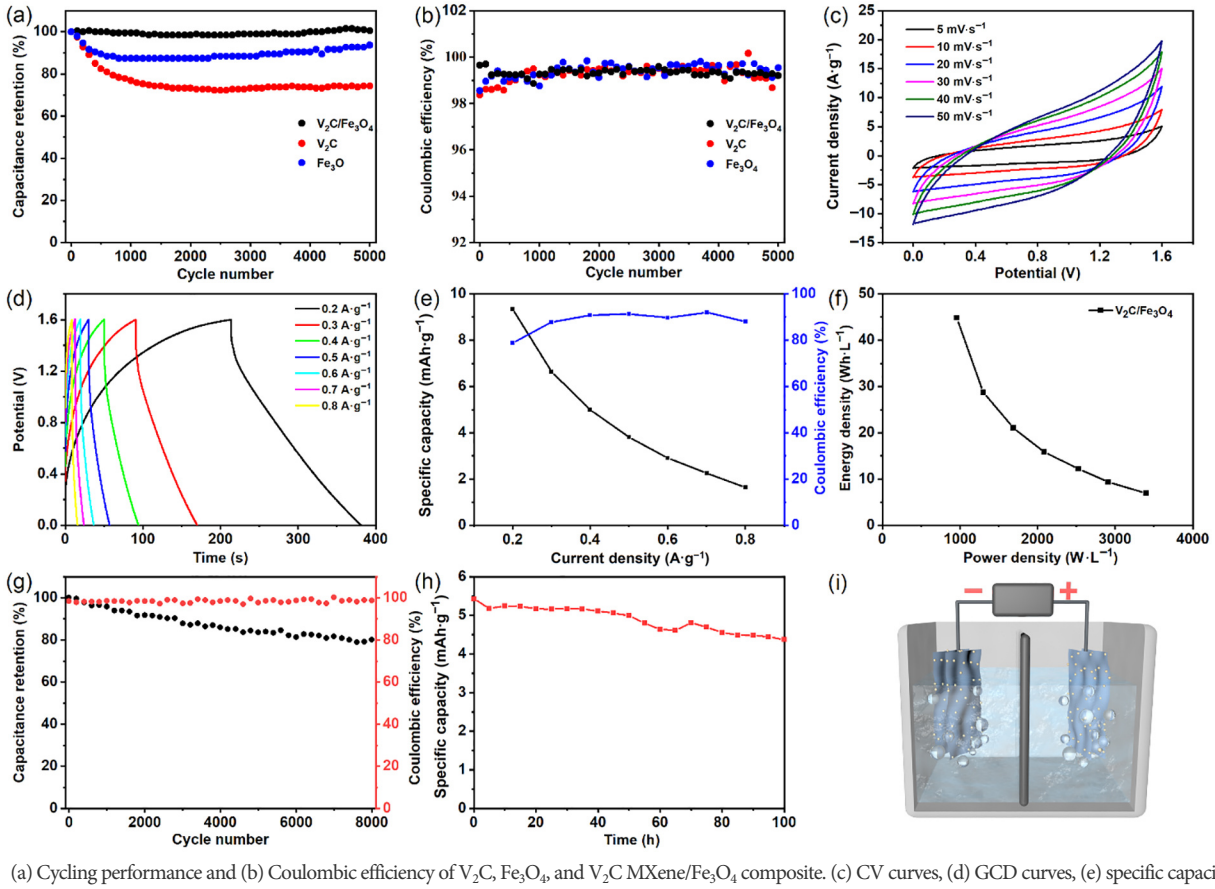


**Fig. 9** (a) Cycling performance and (b) Coulombic efficiency of $V_2C$, $Fe_3O_4$, and $V_2C$ MXene/$Fe_3O_4$ composite. (c) CV curves, (d) GCD curves, (e) specific capacity and Coulombic efficiency, (f) Ragone plot, (g) cycling performance and Coulombic efficiency, and (h) specific capacity vs. float time plot of $V_2C$ MXene/$Fe_3O_4$//$V_2C$ MXene/$Fe_3O_4$ SSC device. (i) Schematic of $V_2C$ MXene/$Fe_3O_4$//$V_2C$ MXene/$Fe_3O_4$ configuration.


清華大学出版社 Tsinghua University Press | SciOpen

volumetric energy density of the $V_2C$ MXene/$Fe_3O_4$ SSC device are 959.4 and 44.8 Wh·L$^{-1}$, respectively, confirming its feasibility as a portable electronic device. The volumetric energy density decreases to 7.0 Wh·L$^{-1}$ when the volumetric power density is increased to 3397.1 W·L$^{-1}$. The cycling performance of the $V_2C$ MXene/$Fe_3O_4$ SSC device is shown in Fig. 9(g). At a current density of 0.5 A·g$^{-1}$, the $V_2C$ MXene/$Fe_3O_4$ SSC device achieves a capacitance retention of 80.14% after 8000 cycles, indicating the good chemical stability of the fabricated $V_2C$ MXene/$Fe_3O_4$ SSC device. Similarly, the Coulombic efficiency of the $V_2C$ MXene/$Fe_3O_4$ SSC device is 97%–99% over 8000 cycles. The specific capacity retention of the SSC device reaches 98.74% after 8000 charge–discharge cycles, indicating the extremely high energy conversion efficiency of the considered material during the electrochemical processes. The observed decay in the cycling performance of the $V_2C$ MXene/$Fe_3O_4$ SSC device could be attributed to several factors. One possible factor is the structural degradation of the material during repeated charge–discharge cycles. The $V_2C$ and $Fe_3O_4$ components may undergo changes, such as particle aggregation, oxidation, or loss of active sites, reducing the overall performance of the device. Moreover, the conductivity and stability at the interface between $V_2C$ and $Fe_3O_4$ may change during cycling, increasing the internal resistance and decreasing the electrochemical performance. Another factor could be the incomplete recovery of the electrodes after each cycle, which can result in a reduction in the capacitance and overall cycling stability. Finally, the electrolyte and other components of the device might also contribute to the observed performance decay. Thus, further investigations into the underlying mechanisms of this decay are needed to fully understand the cause of this behavior and to develop strategies to improve the cycling stability of the device. Furthermore, the cycling stability of the SSC device within the voltage window was evaluated on the basis of a floating voltage (holding voltage) test conducted at a potential of 1.6 V and a current density of 0.3 A·g$^{-1}$. After five charge–discharge cycles, the device was subjected to a 5 h voltage hold followed by a rest period and then another charge–discharge cycle test to assess the capacitance loss over 100 h. As shown in Fig. 9(h), the SSC device exhibits approximately 20% capacity loss within this voltage window after 100 h of voltage hold. This level of capacity degradation highlights the challenges posed by extended voltage stress, providing valuable insights into the long-term electrochemical stability of the device and its working voltage window for further optimization. Compared with the power and energy densities obtained from the current research on the performance of MXene-based composites and $Fe_3O_4$ composites in supercapacitors, those of the $V_2C$ MXene/$Fe_3O_4$ composite are considerably greater (Table 2), indicating that the $V_2C$ MXene/$Fe_3O_4$ composite is a promising material for SSCs. Figure 9(i) shows a schematic of the $V_2C$ MXene/$Fe_3O_4$ electrode assembled into an SSC device.

### 3.2 Microwave absorption properties

The real parts ($\varepsilon'$ and $\mu'$) of the dielectric constant and permeability and their imaginary parts ($\varepsilon''$ and $\mu''$) represent the ability of the material to store and lose electromagnetic waves [69,70], respectively. Figure 10(a) shows the values of the dielectric constant and permeability of the $V_2C$ MXene/$Fe_3O_4$ composite at 2–18 GHz. The values of $\varepsilon'$ and $\varepsilon''$ are 5.32–5.81 and 0.69–0.44, respectively, and they slightly decrease with increasing frequency, indicating the good storage capacity and maintenance of the $V_2C$ MXene/$Fe_3O_4$ composite. The decrease in $\varepsilon'$ may be due to the frequency dispersion effect caused by polarization hysteresis at high-frequency electromagnetic fields. The $\mu'$ values decrease in the frequency range of 2–6 GHz and flatten at 6–18 GHz. $\mu''$ exhibits more fluctuations (decreasing from 0.55 to 0.076) at 2–18 GHz. The calculated dielectric loss tangent and the magnetic loss tangent are shown in Fig. 10(b). The magnetic loss tangent is greater than the dielectric loss tangent at 2–18 GHz, indicating that magnetic loss plays a major role in the wave absorption mechanism of the $V_2C$ MXene/$Fe_3O_4$ composite.

The Cole–Cole plot [71] is constructed on the basis of the real

**Table 1** Comparison of electrochemical performances of supercapacitors based on MXenes and $Fe_3O_4$

| Material | Electrolyte | Specific capacitance | Current density | Ref. |
|---|---|---|---|---|
| MnS/$V_2C$ $T_x$ | 1 M KOH | 34.78 mAh·g$^{-1}$ | 1 A·g$^{-1}$ | [56] |
| $VO_2$/$V_2C$ $T_x$ | 1 M KOH | 10.84 mAh·g$^{-1}$ | 1 A·g$^{-1}$ | [57] |
| $Ti_3C_2$ $T_x$-MXene foam | 1 M KOH | 203 F·g$^{-1}$ | 5 A·g$^{-1}$ | [58] |
| $Mn_3O_4$–$Fe_3O_4$@C | 1 M NaCl | 178 F·g$^{-1}$ | 1 A·g$^{-1}$ | [59] |
| $Fe_3O_4$–PC (porous carbon) | 6 M KOH | 21.47 F·g$^{-1}$ | 20 mV·s$^{-1}$ | [60] |
| Fe/$Fe_3O_4$@CNT-CNF (carbon nanotubes-carbon nanofibers) | 1 M KOH | 195 F·g$^{-1}$ | 0.5 A·g$^{-1}$ | [61] |
| $Ti_3C_2$ $T_x$ MXene-PPy | 0.5 M $Na_2SO_4$ | 52.75 F·g$^{-1}$ | 2 mV·s$^{-1}$ | [62] |
| $V_2C$ MXene/$Fe_3O_4$ | 1 M KOH | 256.02 F·g$^{-1}$ (42.67 mAh·g$^{-1}$) | 1 A·g$^{-1}$ | This work |

**Table 2** Comparison of the power and energy densities of supercapacitors with different composite materials

| Supercapacitor | Energy density | Power density | Ref. |
|---|---|---|---|
| $Ti_3C_2$ $T_x$-MXene foam//$MnO_2$ | 16.5 Wh·kg$^{-1}$ | 160 W·kg$^{-1}$ | [58] |
| $Ti_3C_2$ $T_x$-Mn SSC | 38.4 Wh·kg$^{-1}$ | 55.3 W·cm$^{-3}$ | [63] |
| $Mo_2C$/$MoO_3$ SSC | 25 Wh·kg$^{-1}$ | 243 W·kg$^{-1}$ | [64] |
| MXene/PZS SSC | 12.26 Wh·kg$^{-1}$ | 125 W·kg$^{-1}$ | [65] |
| MXene/CNT//MXene ASC | 7.34 Wh·kg$^{-1}$ | 50 W·kg$^{-1}$ | [66] |
| Phenolic resin-$Fe_3O_4$@$MnO_2$ SSC | 25.7 Wh·kg$^{-1}$ | 384.9 W·kg$^{-1}$ | [67] |
| CPY//C-G/carbon-GO/ammonium ferric citrate | 18.3 Wh·kg$^{-1}$ | 351 W·kg$^{-1}$ | [40] |
| Graphene oxide@$Fe_3O_4$@tungstate SSC | 7.38 Wh·kg$^{-1}$ | 40 W·kg$^{-1}$ | [68] |
| $V_2C$ MXene/$Fe_3O_4$ SSC | 44.8 Wh·L$^{-1}$ (20.8Wh·kg$^{-1}$) | 959.4 W·L$^{-1}$ (444.2 W·kg$^{-1}$) | This work |

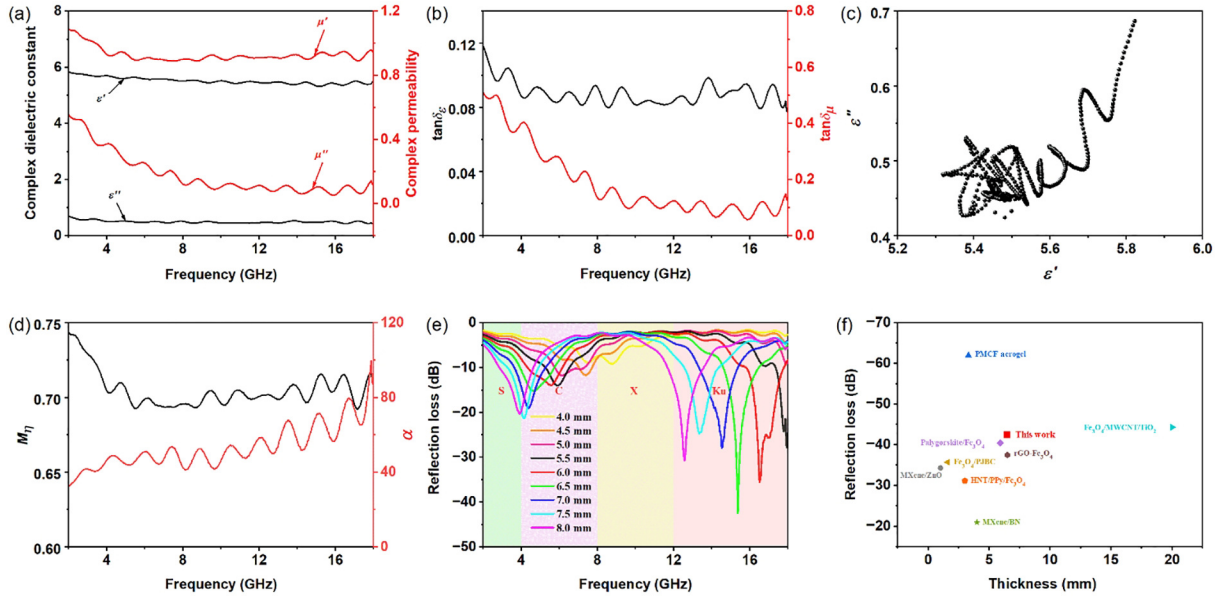


**Fig. 10** Data for $V_2C$ MXene/$Fe_3O_4$ composite: (a) complex permittivity and complex permeability curves, (b) $\tan\delta_\varepsilon$ and $\tan\delta_\mu$ vs. frequency curves, (c) Cole–Cole plot, (d) attenuation constant alongside impedance matching curve, and (e) RL plots. (f) Comparison of reflection losses of $V_2C$ MXene/$Fe_3O_4$, MXene-based, and $Fe_3O_4$-based composites.

and imaginary components of the dielectric constant. Several irregular ellipses are observed in Fig. 10(c). The presence of multiple ellipses suggests that the $V_2C$ MXene/$Fe_3O_4$ composite exhibits multiple Debye relaxation processes, which can be attributed to the heterogeneous interfaces formed between $V_2C$ and $Fe_3O_4$. The dielectric properties of $Fe_3O_4$ contribute to its internal polarization, whereas the diverse functional groups inherent to MXenes generate dipole polarization. The $V_2C$ MXene/$Fe_3O_4$ composites exhibit multiple polarization mechanisms, including interface polarization and dipole alignment, collectively enhancing their dielectric loss characteristics.

Figure 10(d) shows the attenuation constant and impedance matching coefficient determined via Eqs. (7) and (8). As shown in Fig. 10(d), with increasing frequency, the attenuation constant increases, whereas the impedance matching coefficient decreases. These parameters are key indicators of the material absorption properties. An impedance matching coefficient approaching unity indicates minimal reflection and enhanced wave absorption, whereas a high attenuation constant signifies substantial energy loss during wave propagation [72]. Within the Ku band, the $V_2C$ MXene/$Fe_3O_4$ composite material has a relatively high attenuation constant coupled with a wave impedance exceeding 0.7, indicating superior absorption performance within this frequency range.

Figure 10(e) shows a plot of the calculated RL of the $V_2C$ MXene/$Fe_3O_4$ composite at different thicknesses vs. frequency. A material can absorb 90% of the electromagnetic waves when its RL < 10 dB, making it an effective wave-absorbing material. The microwave-absorbing capacity of a material differs in different frequency band ranges. The results show that the absorbing capacity of the $V_2C$ MXene/$Fe_3O_4$ composite in the S and C bands increases with its thickness. The best RL (−20.3 dB) is achieved at 3.92 GHz, with an effective absorption bandwidth of 1.8 GHz (2.8–4.6 GHz). In the X band, almost no microwave absorption is observed. This phenomenon may be attributed to the incomplete manifestation of the ferromagnetic properties of $Fe_3O_4$ within this frequency range, which increases the degree of hysteresis loss. Furthermore, the interaction at the interface between $V_2C$ and $Fe_3O_4$ does not successfully establish an effective absorption mechanism in the X band. In the Ku band, the $V_2C$ MXene/$Fe_3O_4$ composite has strong absorption properties. The $RL_{min}$ of the $V_2C$ MXene/$Fe_3O_4$ composite is 35.5 dB, which is obtained at a frequency of 16.51 GHz and a thickness of 6.0 mm, and the effective absorption bandwidth is 2.0 GHz (15.8–17.8 GHz). The optimum RL (−42.4 dB) is obtained at 15.37 GHz and a thickness of 6.5 mm when the effective absorption bandwidth is 1.9 GHz (14.6–16.5 GHz). As the thickness of the $V_2C$ MXene/$Fe_3O_4$ absorber increases from 6.5 to 8.0 mm, the frequency of the microwave absorption of the material gradually decreases from 15.37 to 12.57 GHz. The impedance matching analysis, attenuation constant curves [73], and RL curves indicate that the attenuation constant of $V_2C$ MXene/$Fe_3O_4$ composites in the S and C bands is comparable to that in the X band. However, the impedance matching observed in the S and C bands is considerably greater than that observed in the X band. Thus, the absorption performance in the X band is inferior to that in the S and C bands. Moreover, the impedance matching and attenuation constant of the composite materials in the Ku band exceeds those in the X band, resulting in better absorption performance in the Ku band than in the X band. Thus, the $V_2C$ MXene/$Fe_3O_4$ composite at different thicknesses has an effective absorption level over the entire Ku band with a high microwave absorption intensity.

Han *et al.* [74] reported that $V_2C$ MXene thin films integrated with a polyurethane matrix exhibited an $RL_{min}$ of −32.9 dB in the X band. This was accompanied by a forbidden bandwidth of 4.2 GHz. In comparison, the paraffin-based $V_2C$ MXene/$Fe_3O_4$ composites presented a considerably lower $RL_{min}$ of −42.4 dB in the Ku band (with a forbidden bandwidth of 1.9 GHz) and an RL of −15.2 dB in the S and C bands (with a forbidden bandwidth of 1.8 GHz).

This study highlights the distinct effects of material morphology and substrate characteristics on wave absorption properties. Thin-film materials typically exhibit larger surface areas, which increase their absorption owing to their improved interfacial polarization [75]. In contrast, powder materials perform through complex mechanisms, which are affected by particle spacing and structural configuration [76]. Moreover, the physicochemical properties of a substrate strongly affect its

material absorption ability, whereas its elasticity and flexibility impose constraints on its structural integrity. Compared with these studies, our findings demonstrate the superior wave absorption performance of $V_2C$ MXene/$Fe_3O_4$ composites in the Ku band, which can be attributed to the synergistic effects of multiple polarization mechanisms and optimized material morphology. In summary, the $V_2C$ MXene/$Fe_3O_4$ composite has a high microwave-absorbing ability and acceptable bandwidth, and its microwave-absorbing properties are apparent mainly within the S and C bands in the low-frequency region and the Ku band in the high-frequency region. The current status of the microwave absorption studies of the MXene-based composites [77–79] and $Fe_3O_4$-based composites [80–84] is shown in Fig. 10(f), and Table 3 presents the microwave-absorbing properties of the relevant materials, with the $V_2C$ MXene/$Fe_3O_4$ composite exhibiting better microwave absorption properties.

**Table 3** Comparison of microwave-absorbing properties of MXene and $Fe_3O_4$ composites

| Material | Thickness (mm) | $RL_{min}$ (dB) | Effective absorption bandwidth (GHz) | Ref. |
|---|---|---|---|---|
| MXene/BN | 4.0 | −20.94 | 9.71 | [77] |
| MXene/ZnO | 1.0 | −34.31 | 3.47 | [78] |
| Polyimide/MXene/carbon fibers | 3.3 | −61.96 | 3.97 | [79] |
| $Fe_3O_4$/$Ti_3C_2$ MXene | 4.2 | −57.20 | 1.40 | [85] |
| HNT/PPy/$Fe_3O_4$ | 3.0 | −31.18 | — | [80] |
| Palygorskite/$Fe_3O_4$ | 5.9 | −40.41 | — | [81] |
| $Fe_3O_4$/porous carbon | 1.6 | −35.70 | 5.00 | [82] |
| $Fe_3O_4$/MWCNT/$TiO_2$ | 20 | −44.30 | — | [83] |
| rGO-$Fe_3O_4$ | 6.5 | −37.50 | 1.90 | [84] |
| $V_2C$ MXene/$Fe_3O_4$ | 6.5 | −42.40 | 1.90 | This work |

The high conductivity of $V_2C$ considerably enhances the charge transfer efficiency of $Fe_3O_4$, which increases the overall rate of electrochemical reactions. Effective charge transfer facilitates polarization reactions within a material, optimizing its electrochemical performance and improving its microwave absorption capabilities. The interface established between $V_2C$ and $Fe_3O_4$ provides the material with additional active sites, promoting its electrochemical reactions and inducing interface polarization, which enhances the material's absorption of electromagnetic waves. $V_2C$ MXene/$Fe_3O_4$ composites demonstrate excellent electrochemical properties and microwave absorption capabilities, allowing them to exhibit effective performance in environments with electromagnetic interference. The microwave absorption characteristics of the $V_2C$ MXene/$Fe_3O_4$ composite material protect it against overheating due to electromagnetic interference, which enhances the energy density and cycling stability of $V_2C$ MXene/$Fe_3O_4$-based devices operating in such environments. This research offers innovative strategies for the design and optimization of supercapacitors and paves the way for the development of advanced devices, such as energy storage systems, electric vehicles, and portable electronics, that require efficient electromagnetic wave absorption and stable performance in electromagnetic interference-prone environments.

## 4 Conclusions

Herein, a $V_2C$ MXene/$Fe_3O_4$ composite was successfully prepared via a self-assembly method using $V_2C$ MXene and $Fe_3O_4$ nanoparticles as raw materials. The combination of the $V_2C$ MXene lamellar structure with $Fe_3O_4$ nanoparticles results in a high specific capacity and excellent electrochemical stability. The prepared $V_2C$ MXene/$Fe_3O_4$//$V_2C$ MXene/$Fe_3O_4$ supercapacitors exhibit excellent Coulombic efficiencies at different current densities, achieving energy and power densities of 44.8 $Wh{\cdot}L^{-1}$ and 959.4 $W{\cdot}L^{-1}$, respectively. Furthermore, the $V_2C$ MXene/$Fe_3O_4$ composite exhibited excellent microwave absorption properties with a high overall microwave absorption ability and acceptable bandwidth. Therefore, the proposed $V_2C$ MXene/$Fe_3O_4$ composite can be widely employed in electrochemical devices and as a microwave absorption material.

### Competing interests

The authors have no competing interests to declare that are relevant to the content of this article. The author Aiguo Zhou is the Associate Editor of this journal.

### Acknowledgements

This study was supported by the National Natural Science Foundation of China (Nos. 52372284 and 52275187), the Fundamental Research Funds for the Universities of Henan Province (Nos. NSFRF210326 and NSFRF200101), the Natural Science Foundation of Henan Province (Nos. 232300421135 and 232300421204), and the Doctoral Fund Project of Henan Polytechnic University (No. B2019-41). The authors would like to thank Jiaxiu Zhou from the Shiyanjia Laboratory (www.shiyanjia.com) for the TEM analysis.

### References

[1] Novoselov KS, Geim AK, Morozov SV, *et al.* Electric field effect in atomically thin carbon films. *Science* 2004, **306**: 666–669.

[2] Mason MJ, Coleman BJ, Saha S, *et al.* Graphene signatures: Identifying graphite and graphene grades via radio frequency heating. *Carbon* 2021, **182**: 564–570.

[3] Wang Y, Huang K, Derré A, *et al.* Conductive graphene coatings synthesized from graphenide solutions. *Carbon* 2017, **121**: 217–225.

[4] Wang CJ, Xu QF, Hu JR, *et al.* Graphene/SiC-coated textiles with excellent electromagnetic interference shielding, Joule heating, high-temperature resistance, and pressure-sensing performances. *J Adv Ceram* 2023, **12**: 778–791.

[5] Wang X, Xia Y, Huang JT, *et al.* A facile strategy for large-scale production of 2D nanosheets exfoliated by three-roll milling. *J Adv Ceram* 2024, **13**: 11–18.

[6] Ben-Shimon Y, Bhingardive V, Joselevich E, *et al.* Self-sensing $WS_2$ nanotube torsional resonators. *Nano Lett* 2022, **22**: 8025–8031.

[7] Tang HL, Chiu MH, Tseng CC, *et al.* Multilayer graphene-$WSe_2$ heterostructures for $WSe_2$ transistors. *ACS Nano* 2017, **11**: 12817–12823.

[8] Zhong QJ. Intrinsic and engineered properties of black phosphorus. *Mater Today Phys* 2022, **28**: 100895.

[9] Jaffe GR, Smith KJ, Watanabe K, *et al.* Thickness-dependent cross-

plane thermal conductivity measurements of exfoliated hexagonal boron nitride. *ACS Appl Mater Inter* 2023, **15**: 12545–12550.
[10] Yu L, Deng MD, Zhang JL, *et al.* Site-controlled quantum emitters in monolayer $MoSe_2$. *Nano Lett* 2021, **21**: 2376–2381.
[11] Xia QX, Xu JY, Liu KK, *et al.* In-situ growth and DFT analysis of nickel halide nanostructures for enhanced electrochemical supercapacitors. *J Alloys Compd* 2025, **1010** : 178018.
[12] Si LJ, Xia QX, Liu KK, *et al.* Hydrothermal synthesis of layered $NiS_2$/$Ti_3C_2T_x$ composite electrode for supercapacitors. *Mater Chem Phys* 2022, **291**: 126733.
[13] Zheng ZX, Wu W, Yang T, *et al. In situ* reduced MXene/AuNPs composite toward enhanced charging/discharging and specific capacitance. *J Adv Ceram* 2021, **10**: 1061–1071.
[14] Liu J, Xia QX, Wang LB, *et al. In situ* growth of nanorod-shaped Ni, Co-MOF on $Mo_2CT_x$ MXene surface to realize enhanced energy storage for supercapacitors. *ACS Appl Mater Inter* 2024, **16**: 49380–49391.
[15] Zhao TB, Lan D, Jia ZR, *et al.* Hierarchical porous molybdenum carbide synergic morphological engineering towards broad multi-band tunable microwave absorption. *Nano Res* 2024, **17**: 9845–9856.
[16] Sun C, Lan D, Jia Z, *et al.* Kirkendall effect-induced ternary heterointerfaces engineering for high polarization loss MOF-LDH-MXene absorbers. *Small* 2024, **20**: 2405874.
[17] Zhang Y, Lan D, Hou TQ, *et al.* Multifunctional electromagnetic wave absorbing carbon fiber/$Ti_3C_2T_x$ MXene fabric with ultra-wide absorption band. *Carbon* 2024, **230**: 119594.
[18] Alwarappan S, Nesakumar N, Sun DL, *et al.* 2D metal carbides and nitrides (MXenes) for sensors and biosensors. *Biosens Bioelectron* 2022, **205**: 113943.
[19] Zhang HX, Wang ZH, Zhang QX, *et al.* $Ti_3C_2$ MXenes nanosheets catalyzed highly efficient electrogenerated chemiluminescence biosensor for the detection of exosomes. *Biosens Bioelectron* 2019, **124**: 184–190.
[20] Zhu C, Liang JX, Wang YG, *et al.* Non-noble metal single-atom catalyst with MXene support: $Fe_1/Ti_2CO_2$ for CO oxidation. *Chinese J Catal* 2022, **43**: 1830–1841.
[21] De S, Roy S, Nayak GC. $MoSn_2Se_4$-decorated MXene/functionalized RGO nanohybrid for ultrastable supercapacitor and oxygen evolution catalyst. *Mater Today Nano* 2023, **22**: 100337.
[22] Li Y, Qing YC, Zhang YR, *et al.* Simultaneously tuning structural defects and crystal phase in accordion-like $Ti_xO_{2x-1}$ derived from $Ti_3C_2T_x$ MXene for enhanced electromagnetic attenuation. *J Adv Ceram* 2023, **12**: 1946–1960.
[23] Guo YT, Zhang X, Jin S, *et al.* Synthesis of $Mo_2C$ MXene with high electrochemical performance by alkali hydrothermal etching. *J Adv Ceram* 2023, **12**: 1889–1901.
[24] Xu WK, Shi ZN, Yu ZY, *et al.* A sweet synthesis of MXenes. *Nano Lett* 2024, **24**: 10547–10553.
[25] Zhang H, Yang L, Zhang PG, *et al.* MXene-derived $Ti_nO_{2n-1}$ quantum dots distributed on porous carbon nanosheets for stable and long-life Li–S batteries: Enhanced polysulfide mediation via defect engineering. *Adv Mater* 2021, **33**: 2008447.
[26] Sha DW, Lu CJ, He W, *et al.* Surface selenization strategy for $V_2CT_x$ MXene toward superior Zn-ion storage. *ACS Nano* 2022, **16**: 2711–2720.
[27] Zheng W, Yang L, Wang LX, *et al.* MXene nanomesh for high-performance supercapacitor. *J Alloys Compd* 2024, **976**: 173065.
[28] Liu Y, Ren XY, Zhou XF, *et al.* Defect design and vacancy engineering of $NiCo_2Se_4$ spinel composite for excellent electromagnetic wave absorption. *Ceram Int* 2024, **50**: 46643–46652.
[29] Zhu JH, Lan D, Liu XH, *et al.* Porous structure fibers based on multi-element heterogeneous components for optimized electromagnetic wave absorption and self-anticorrosion performance. *Small* 2024, **20**: 2403689.
[30] Zeng XJ, Jiang X, Ning Y, *et al.* Construction of dual heterogeneous interface between zigzag-like Mo–MXene nanofibers and small CoNi@NC nanoparticles for electromagnetic wave absorption. *J Adv Ceram* 2023, **12**: 1562–1576.
[31] Miao RL, Xia QX, Wang LB, *et al.* Insight on electronic and thermal behaviors of conductive MXene-based composite material and their electromagnetic shielding Applications: A Review. *FlatChem* 2025, **49**: 100782.
[32] Zhang YJ, Hu RX, Zhang PG, *et al.* Gravity-induced single-layer gradient structure of Ni@$Ti_3C_2T_x$/PVA for enhanced microwave absorption. *J Mater Chem A* 2023, **11**: 5873–5882.
[33] Zhang YJ, Han MK, Hu RX, *et al.* Sandwiched MXene/polyimide composite foams for multiscale microwave absorption. *Sci China Mater* 2024, **67**: 272–278.
[34] Han MK, Gogotsi Y. Perspectives for electromagnetic radiation protection with MXenes. *Carbon* 2023, **204**: 17–25.
[35] Narayanan TM, Zhu YG, Gençer E, *et al.* Low-cost manganese dioxide semi-solid electrode for flow batteries. *Joule* 2021, **5**: 2934–2954.
[36] Tang YJ, Zheng SS, Xu YX, *et al.* Advanced batteries based on manganese dioxide and its composites. *Energy Storage Mater* 2018, **12**: 284–309.
[37] Eftekhari A, Li L, Yang Y. Polyaniline supercapacitors. *J Power Sources* 2017, **347**: 86–107.
[38] Zhang BF, Zhou PF, Xu YL, *et al.* Gravity-assisted synthesis of micro/nano-structured polypyrrole for supercapacitors. *Chem Eng J* 2017, **330**: 1060–1067.
[39] Low WH, Khiew PS, Lim SS, *et al.* Recent development of mixed transition metal oxide and graphene/mixed transition metal oxide based hybrid nanostructures for advanced supercapacitors. *J Alloys Compd* 2019, **775**: 1324–1356.
[40] Fan H, Niu R, Duan J, *et al.* $Fe_3O_4$@carbon nanosheets for all-solid-state supercapacitor electrodes. *ACS Appl Mater Inter* 2016, **8**: 19475–19483.
[41] Li X, Shao CL, Wang XL, *et al.* Preparation of $Fe_3O_4$/$Fe_xS_y$ heterostructures via electrochemical deposition method and their enhanced electrochemical performance for lithium-sulfur batteries. *Chem Eng J* 2022, **446**: 137267.
[42] Zhu XZ, Hou D, Tao HS, *et al.* Simply synthesized N-doped carbon supporting $Fe_3O_4$ nanocomposite for high performance supercapacitor. *J Alloys Compd* 2020, **821**: 153580.
[43] Shi YN, Gao XH, Qiu J. Synthesis and strengthened microwave absorption properties of three-dimensional porous $Fe_3O_4$/graphene composite foam. *Ceram Int* 2019, **45**: 3126–3132.
[44] Zhang YH, Lv XY, Zhang Y, *et al.* Tunable microwave absorbing property of RGO/$Fe_3O_4$/$SiO_2$ nanocomposites by effective regulation of eddy current effect. *J Appl Phys* 2021, **130**: 175101.
[45] Xiang Y, Zhou JW, Liu JH, *et al.* High-performance CF/MXene/β-$PbO_2$ materials as anodes for asymmetric supercapacitors. *Ceram Int* 2024, **50**: 3829–3836.
[46] Du XY, Wang LB, Fu YW, *et al.* Enhancing the electrochemical performance of d-$Mo_2$CTx MXene in lithium-ion batteries and supercapacitors by sulfur decoration. *Ceram Int* 2023, **49**: 19737–19745
[47] Althubiti NA, Aman S, Taha TAM. Synthesis of $MnFe_2O_4$/MXene/NF nanosized composite for supercapacitor application. *Ceram Int* 2023, **49**: 27496–27505.
[48] Bai WY, Yong ZP, Wang S, *et al.* Polyaniline-MXene composite electrode with excellent electrochemical properties for all-solid flexible supercapacitors. *J Energy Storage* 2023, **71**: 108053.
[49] Liu KK, Xia QX, Si LJ, *et al.* Defect engineered $Ti_3C_2T_x$ MXene electrodes by phosphorus doping with enhanced kinetics for supercapacitors. *Electrochim Acta* 2022, **435**: 141372.
[50] Cheng YH, Lan D, Jia ZR, *et al.* MOF derivatives anchored to multichannel hollow carbon fibers with gradient structures for corrosion resistance and efficient electromagnetic wave absorption. *J Mater Sci Technol* 2025, **216**: 150–164.
[51] Han MJ, Lan D, Zhang ZM, *et al.* Micro-sized hexapod-like CuS/$Cu_9S_5$ hybrid with broadband electromagnetic wave absorption. *J Mater Sci Technol* 2025, **214**: 302–312.
[52] Guo ZQ, Lan D, Jia ZR, *et al.* Multiple tin compounds modified

carbon fibers to construct heterogeneous interfaces for corrosion prevention and electromagnetic wave absorption. *Nano-micro Lett* 2024, **17**: 23.
[53] Wang YS, Li YY, Qiu ZP, *et al.* $Fe_3O_4$@$Ti_3C_2$ MXene hybrids with ultrahigh volumetric capacity as an anode material for lithium-ion batteries. *J Mater Chem A* 2018, **6**: 11189–11197.
[54] Zhou AG, Liu Y, Li SB, *et al.* From structural ceramics to 2D materials with multi-applications: A review on the development from MAX phases to MXenes. *J Adv Ceram* 2021, **10**: 1194–1242.
[55] Akhtar S, Singh J, Tran TT, *et al.* Synthesis and optical properties of light-emitting V2N MXene quantum dots. *Opt Mater* 2023, **138**: 113660.
[56] Shen FX, Xia QX, Chang YK, *et al.* Spherical γ-MnS decorated $V_2C$ MXene for powering portable devices. *J Energy Storage* 2024, **104**: 114434.
[57] Zhu ZY, Xia QX, Wang LB, *et al. In situ* grown $VO_2$/$V_2C$ MXene and its supercapacitor applications. *J Energy Storage* 2024, **88**: 111484.
[58] Zhu YC, Rajouâ K, Le Vot S, *et al.* Modifications of MXene layers for supercapacitors. *Nano Energy* 2020, **73**: 104734.
[59] Hu B, Wang YB, Shang XH, *et al.* Structure-tunable $Mn_3O_4$–$Fe_3O_4$@C hybrids for high-performance supercapacitor. *J Colloid Interf Sci* 2021, **581**: 66–75.
[60] Li YC, Xu MD, Yin HS, *et al.* Yolk–shell $Fe_3O_4$ nanoparticles loaded on persimmon-derived porous carbon for supercapacitor assembly and as (V) removal. *J Alloys Compd* 2019, **810**: 151887.
[61] Aftab F, Tanveer S, Rehman SU, *et al.* Encapsulation of Fe/$Fe_3O_4$ in carbon nanotubes grown over carbon nanofibers for high performance supercapacitor electrodes. *Synthetic Met* 2020, **269**: 116575.
[62] Liang WY, Zhitomirsky I. MXene-polypyrrole electrodes for asymmetric supercapacitors. *Electrochim Acta* 2022, **406**: 139843.
[63] Xu HJ, Fan J, Su H, *et al.* Metal ion-induced porous MXene for all-solid-state flexible supercapacitors. *Nano Lett* 2023, **23**: 283–290.
[64] Xu HJ, Dong HL, Liu XT, *et al.* High-temperature oxidized $Mo_2CT_x$ MXene for a high-performance supercapacitor. *ACS Appl Mater Inter* 2023, **15**: 53549–53557.
[65] Li L, Niu H, Robertson J, *et al.* Cyclocrosslinked polyphosphazene modified MXene as aqueous supercapacitor. *Electrochim Acta* 2023, **439**: 141574.
[66] Shi X, Guo FM, Hou KH, *et al.* Highly flexible all-solid-state supercapacitors based on MXene/CNT composites. *Energ Fuel* 2023, **37**: 9704–9712.
[67] Dong XX, Wang JY, Miao JF, *et al.* $Fe_3O_4$/$MnO_2$ co-doping phenolic resin porous carbon for high performance supercapacitors. *J Taiwan Inst Chem E* 2022, **135**: 104385.
[68] Dalvand S, Khoushab Z, Mousavi-Khoshdel SM, *et al.* Graphene oxide@$Fe_3O_4$@Tungstate modified ionic liquid as a novel electrode material for high-performance supercapacitor. *Int J Hydrogen Energy* 2023, **48**: 10098–10107.
[69] Qiao LJ, Bi JQ, Liang GD, *et al.* Synthesis of high-entropy MXenes with high-efficiency electromagnetic wave absorption. *J Adv Ceram* 2023, **12**: 1902–1918.
[70] Jia ZR, Sun LF, Gao ZG, *et al.* Modulating magnetic interface layer on porous carbon heterostructures for efficient microwave absorption. *Nano Res* 2024, **17**: 10099–10108.
[71] Peng HL, Xiong ZQ, Gan ZH, *et al.* Microcapsule MOFs@MOFs derived porous "nut-bread" composites with broadband microwave absorption. *Compos Part B-Eng* 2021, **224**: 109170.
[72] Cai B, Zhou L, Zhao PY, *et al.* Interface-induced dual-pinning mechanism enhances low-frequency electromagnetic wave loss. *Nat Commun* 2024, **15**: 3299.
[73] Hou ZL, Gao XS, Zhang JY, *et al.* A perspective on impedance matching and resonance absorption mechanism for electromagnetic wave absorbing. *Carbon* 2024, **222**: 118935.
[74] Han M, Shuck CE, Singh A, *et al.* Efficient microwave absorption with $V_{n+1}C_nT_x$ MXenes. *Cell Rep Phys Sci* 2022, **3**: 101073.
[75] Zhao XX, Huang Y, Jiang HY, *et al.* Designed $MoSe_2$ modified multi-layer hollow carbon fiber composite material achieves tunable electromagnetic wave absorption in the X and Ku bands. *Carbon* 2024, **224**: 119063.
[76] Li ZL, Tian XX, Wang JF, *et al.* Facial synthesis of $MgFe_2O_4$/MWCNT nanocomposite powders as an effective wave-absorbing material with ultrathin thickness. *ACS Appl Nano Mater* 2025, **8**: 1727–1737.
[77] Li N, Huang GW, Xiao HM, *et al.* Investigations on structure-dependent microwave absorption performance of nano-$Fe_3O_4$ coated carbon-based absorbers. *Carbon* 2019, **144**: 216–227.
[78] Huang YF, Xie YL, Zhao J, *et al.* Variety of ZIF-8/MXene-based lightweight microwave-absorbing materials: Preparation and performances of ZnO/MXene nanocomposites. *The Journal of Physical Chemistry C* 2022, **126**: 13847–13853.
[79] Chao M, Chu N, Zhang B, *et al.* MXene/carbon fiber/polyimide composite aerogel for multifunctional microwave absorption. *Compos Commun* 2024, **46**: 101837.
[80] Maleki ST, Babamoradi M, Rouhi M, *et al.* Facile hydrothermal synthesis and microwave absorption of halloysite/polypyrrole/$Fe_3O_4$. *Synthetic Met* 2022, **290**: 117142.
[81] Wang S, Ren HD, Lian W, *et al.* Purification and dissociation of raw palygorskite through wet ball milling as a carrier to enhance the microwave absorption performance of $Fe_3O_4$. *Appl Clay Sci* 2021, **200**: 105915.
[82] Wang LH, Guan HT, Hu JQ, *et al.* Jute-based porous biomass carbon composited by $Fe_3O_4$ nanoparticles as an excellent microwave absorber. *J Alloys Compd* 2019, **803**: 1119–1126.
[83] Qoidah SN, Ulfawanti Intan Subadra S, Taufiq A, *et al.* $Fe_3O_4$/MWCNT/$TiO_2$ nanocomposites as excellent microwave absorber material. *J Alloys Compd* 2024, **970**: 172590.
[84] Du ZH, Chen XB, Zhang YW, *et al.* One-pot hydrothermal preparation of $Fe_3O_4$ decorated graphene for microwave absorption. *Materials* 2020, **13**: 3065.
[85] Zhang X, Wang HH, Hu R, *et al.* Novel solvothermal preparation and enhanced microwave absorption properties of $Ti_3C_2T_x$ MXene modified by *in situ* coated $Fe_3O_4$ nanoparticles. *Appl Surf Sci* 2019, **484**: 383–391.